AIMS Mathematics, 11(4): 9041–9065.
DOI: 10.3934/math.2026373
Received: 21 December 2025
Revised: 03 March 2026
Accepted: 10 March 2026
Published: 02 April 2026

https://www.aimspress.com/journal/Math

Research article

Magnetohydrodynamic flow and heat transfer of a ternary hybrid nanofluid over an expanding porous sheet: Numerical, entropy, and ANN analysis

Abdulaziz H Alharbi*

Mathematics Department, Faculty of Sciences, Umm Al-Qura University, Makkah 21955, Saudi Arabia

* **Correspondence:** Email: ahhrbe@uqu.edu.sa.

Abstract: This study investigates magnetohydrodynamic (MHD) boundary-layer flow, heat transfer, and entropy generation in a ternary hybrid nanofluid composed of Cu–MoS_2 − GO nanoparticles dispersed in an ethylene glycol-water mixture flowing over an expanding porous sheet. Using similarity transformations, the governing partial differential equations are reduced to a coupled system of nonlinear ordinary differential equations and solved numerically. The effects of key physical parameters-including magnetic field strength, nanoparticle volume fraction, particle shape, porous expansion rate, and unsteadiness-on velocity, temperature, skin friction, Nusselt number, and entropy generation are examined in detail. In addition, an artificial neural network (ANN) model is developed to accurately predict the flow and thermal characteristics, demonstrating excellent agreement with numerical results. The findings reveal that nanoparticle shape and concentration significantly influence heat transfer and entropy production, while magnetic and slip effects suppress momentum transport. The combined numerical and ANN-based framework provides an efficient and reliable tool for analyzing complex MHD nanofluid systems.

Keywords: partial differential equations; mathematical modeling; machine learning; MHD boundary layer; heat transfer; numerical method

Nomenclature

B_t Biot number
S_n Slip parameter
D Relaxation parameter
S_p Unsteadiness parameter
E_t Eckert number
M Magnetic parameter

P_S Porosity parameter
P_r Prandtl number
p Shape factor of nanoparticles
s_0 and s_1 Viscosity enhancement coefficients
N_g Entropy generation number
η Similarity variable
u, v, w Velocity components
θ Dimensionless temperature
Re Local Reynolds number
Cf Local skin friction coefficient
Nu Nusselt number
T Temperature of the fluid
T_r Reference temperature
T_∞ Ambient (far-field) temperature
T_w Wall temperature
U_w Wall (stretching) velocity
P Pressure
$\delta_{1,2,3,4,5}$ Constants
α Thermal diffusivity
ψ Stokes stream function
f Dimensionless velocity
σ Electrical conductivity
ν Kinematic viscosity
φ_{thnf} Nanoparticle volume fraction
ρ Density
k Thermal conductivity
μ Viscosity
B_0 Magnetic field
C_p Specific heat

1. Introduction

Modelling heat transfer in nanofluids constitutes a significant challenge in applied mathematics, necessitating advanced techniques to accurately capture the complicated interactions among fluid mechanics, heat transfer, and nanoparticle dynamics. The idea of improving the thermal conductivity of regular heat transfer fluids by adding solid nanoparticles was first used by [1], which started a new type of mathematical models in thermal fluid dynamics. This seminal study created new chances for advanced frameworks that explain the peculiar way heat moves in nanofluid systems. The continuity equation, momentum equations (Navier-Stokes), and energy equations are all well-known partial differential equations that govern traditional heat transfer problems. However, using nanoparticles means that new mathematical models must take into account the new ways that particles can move. In the mathematical modeling of nanofluids, [2] formulated an extensive two-phase model grounded in

the conservation equations for mass, momentum, and energy. This model introduced supplementary transport equations to address variations in nanoparticle concentration, integrating Brownian diffusion and thermophoresis as the principal transport mechanisms.

Magnetohydrodynamic (MHD) nanofluid flows becomes complex because it couples electromagnetic and fluid dynamics equations. By using the Tiwari-Das framework to include nanoparticle effects in the system equations, [3] developed complex mathematical models for free convection in porous media saturated with nanofluids.

The examination of boundary layer theory for nanofluid flows over stretching surfaces has resulted in significant advances in applied mathematics. The study by [4] highlighted mathematical models for carbon nanotube nanofluids, where the system of partial differential equations were transformed into ordinary differential equations with the help of similarity transformation techniques. In addition, the research by [5] describes how viscoelastic nanofluids behave and how nanoparticles move through them. It integrates the Maxwell model for viscoelasticity with the nanofluid transport equations, producing a highly nonlinear system of partial differential equations solved using similarity transformations. Furthermore, [6] explained the efficacy of analytical methods in dealing with nonlinear systems of differential equations prevalent in MHD nanofluid challenges and offered insights into the convergence behaviour and solution structure of these complicated systems.

Mathematical modelling in hybrid nanofluid modelling has received more attention, where multiple types of nanoparticles are dispersed within the base fluid. [7] formulated mathematical models combining homogeneous and heterogeneous chemical reactions, imposing the solution of additional reaction diffusion equations coupled with the equations of fluid dynamics and heat transfer. The framework showed the significance of dimensional analysis and scaling in understanding the relative importance of different physical mechanisms. Furthermore, the research conducted by [8] developed a model of the conjugate heat transfer problem. The authors used the simultaneous solution of the fluid flow equations in the nanofluid domain and the heat conduction equations in the solid boundaries, coupled through suitable interface conditions. [9] created models containing thermodynamic analysis, and the equations of entropy generation result from the second law of thermodynamics and were combined with both equations of fluid flow and heat transfer. There is a mathematical model for ternary hybrid nanofluid systems that has been developed by [10], where three different types of nanoparticles are suspended in a ground fluid. The difficulty of describing such systems is due to the need to solve the coupled transport equations for each type of nanoparticle and the modified fluid dynamics equations at the same time. Advanced numerical methods have been developed to address the complex systems of partial differential equations in nanofluid modelling. [11] employed computational fluid dynamics (CFD) methods along with heat transfer investigation. The purpose is to use advanced numerical methods to split the governing equations in space and time.

The use of artificial neural networks (ANNs) for mathematical modelling in nanofluid research has received a lot of attention. [12] used ANN to predict the thermal characteristics of ternary nanofluids. The authors explored how machine learning algorithms work with classical models based on differential equations. In addition, [13] established a hybrid model that mixed a model containing differential equations with artificial neural networks. This model displays how optimization theory can be used with physics-based models to improve the design and performance for a system. Despite the growing use of artificial intelligence in thermal systems, its integration with entropy-based

analysis of ternary hybrid nanofluids under MHD conditions remains limited.

Motivated by these observations, this study investigates the magnetohydrodynamic flow, heat transfer, and entropy generation of a $Cu–MoS_2 - GO$ ternary hybrid nanofluid over an expanding porous surface. The governing equations are transformed using similarity variables and solved numerically to analyze the effects of magnetic field strength, nanoparticle characteristics, unsteadiness, slip, and porous medium parameters. An artificial neural network is further employed to predict key transport quantities, demonstrating strong agreement with the numerical results. The findings provide useful insight into the thermal and entropic behaviour of MHD ternary hybrid nanofluid flows relevant to advanced heat-transfer applications.

A practical setting where the present analysis becomes relevant is in magnetically assisted coating and thin-film fabrication processes that involve electrically conducting hybrid nanofluids. In many modern coating technologies, porous or deformable substrates are exposed to nanofluid layers while external magnetic fields are used to influence particle distribution, enhance surface uniformity, and assist in heat removal during processing. The ternary combination of $Cu - MoS_2 - GO$ nanoparticles is particularly attractive in this context because copper improves thermal conduction, MoS_2 contributes lubricating and stability characteristics, and graphene oxide provides a large surface area that promotes dispersion and heat spreading. Slip effects may arise due to microstructured or chemically treated surfaces, while porous expansion can represent substrate swelling, chemical interaction, or deformation during operation. Within such processes, entropy generation analysis offers a useful way to quantify irreversibility and identify operating conditions that reduce energy losses and thermal stresses. Moreover, the ANN-based predictive framework developed in this work can serve as a fast surrogate tool for estimating transport behavior, which is beneficial for process monitoring and optimization in industrial coating applications.

While several studies have investigated MHD nanofluid flows, entropy generation, or machine-learning-based prediction techniques independently, our investigation work brings these elements together within a single unified framework. In particular, the study considers an unsteady radial flow of a $Cu–MoS_2 - GO$ ternary hybrid nanofluid over an expanding porous surface, incorporates nanoparticle shape-dependent thermophysical modeling, and performs a detailed entropy generation analysis that accounts simultaneously for magnetic dissipation, viscous effects, and porous resistance. Furthermore, a compact ANN surrogate model is developed and validated against the full numerical dataset to provide rapid predictive capability. Our comprehensive approach allows not only physical interpretation but also practical predictive capability for complex thermal-fluid systems.

2. Problem description

We consider an unsteady, two-dimensional magnetohydrodynamic flow of a ternary hybrid nanofluid composed of Cu, MoS_2, and GO nanoparticles dispersed in an ethylene glycol-water base fluid. The flow is generated by a radially expanding porous surface. A uniform magnetic field of strength B_0 is applied perpendicular to the surface (in the z direction). The induced magnetic field is neglected under the assumption of a small magnetic Reynolds number.

The nanofluid is assumed to be incompressible, electrically conducting, and in thermal equilibrium, with no relative motion between the base fluid and the nanoparticles. Viscous dissipation, Joule heating, and entropy generation effects are inluded into our analysis. The porous

surface allows suction or injection, and a velocity slip condition is imposed at the wall. In the present laminar boundary-layer regime, inertial porous effects are assumed to be negligible, and therefore the Darcy resistance model is adopted instead of the full Darcy–Forchheimer formulation. Thermal interaction between the surface and the fluid is modelled using a convective boundary condition. Owing to rotational symmetry, cylindrical coordinates (r, z) are employed, where r denotes the radial coordinate along the surface and z is normal to it. The corresponding velocity components are denoted by u and w, respectively. Figure 1 illustrates the physical setup of our study. The radial stretching velocity $U_w = br/(1 - ct)$ drives the flow. Here, b is the characteristic stretching rate, c is the dimensional unsteadiness parameter, and $0 \leq ct < 1$. The surface temperature is given by

$$T_w = T_\infty + T_r \frac{br^2}{\nu_f (1 - ct)^2},$$

where T_∞ is the ambient temperature.

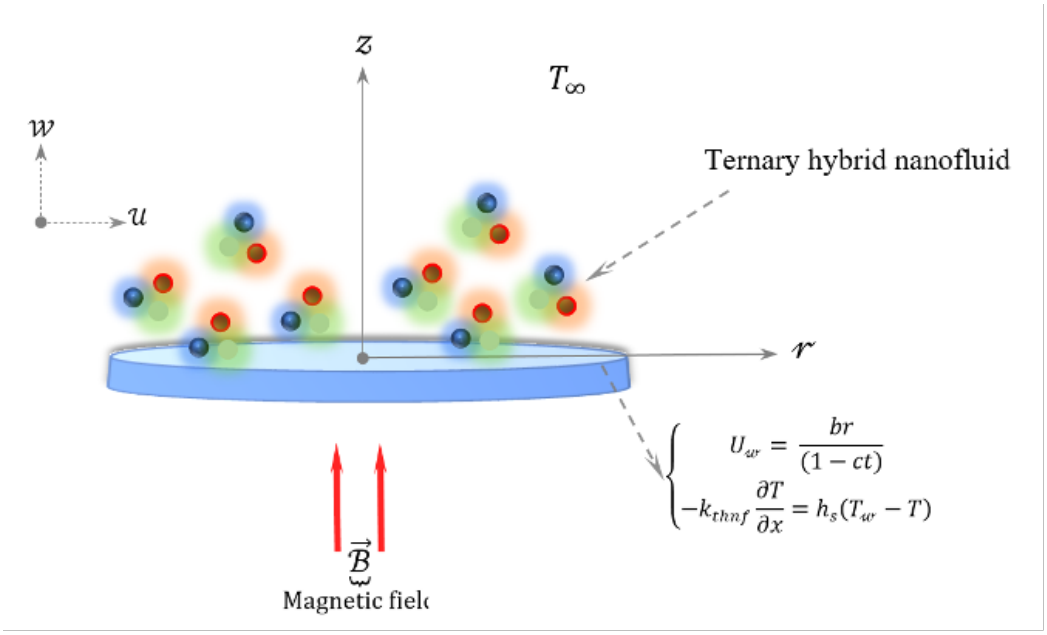

Figure 1. The physical flow model and model setup employed throughout our analysis.

The effective thermophysical properties of the ternary hybrid nanofluid (e.g., density, viscosity, thermal conductivity, electrical conductivity, and specific heat) are denoted by the subscript "thnf" and are defined using standard mixture models, as summarized in Tables 2 and 3. Our study considers a radial stretching velocity $\sim br/(1 - ct)$ that represents the axisymmetric analog of the classical stretching-sheet model introduced by [14] for planar flows. In many practical situations, however, surface deformation occurs radially rather than in a single Cartesian direction. Examples include circular coating and deposition processes, thin-film growth on expanding substrates, polymer sheet stretching with axisymmetric strain, and membrane systems where suction or injection is applied uniformly across a circular surface. In such configurations, the surface velocity scales linearly with the radial coordinate, leading to a velocity proportional to the radius, r. The present formulation therefore extends the well-established stretching-sheet approach to an unsteady cylindrical geometry

while preserving similarity structure and enabling thermodynamic analysis of porous and magnetically influenced nanofluid flows.

Our study uses a few assumptions that make our analysis tractable. First of all, the flow is assumed to be two-dimensional, unsteady, incompressible, and axisymmetric. Next, the ternary hybrid nanofluid is composed of Cu–$MoS_2 - GO$ nanoparticles that are uniformly dispersed in the H_2 O-ethylene glycol mixtures (EG<50%>$-H_2O$<50%>). The magnetic field of the form $B = B_0/(1-ct)^{1/2}$ is applied along the z-axis, and Joule heating effects are incorporated into the energy equation. A velocity slip boundary condition is imposed at the surface of the porous sheet to represent the non-continuous behavior of the fluid near the boundary. Finally, the heat transfer at the surface occurs through convection and is characterized by a constant heat transfer coefficient.

The fundamental equations governing continuity, Navier-Stokes, and energy equations for this configuration are expressed as

$$\frac{1}{r}\frac{\partial(ru)}{\partial r} + \frac{\partial w}{\partial z} = 0, \tag{2.1}$$

$$\frac{\partial u}{\partial t} + u\frac{\partial u}{\partial r} + w\frac{\partial u}{\partial z} = \frac{\mu_{thnf}}{\rho_{thnf}}\frac{\partial^2 u}{\partial z^2} - \frac{\sigma_{thnf}B^2 u}{\rho_{thnf}} - \frac{\mu_{thnf}}{\rho_{thnf}k^*}u, \tag{2.2}$$

$$\frac{\partial T}{\partial t} + u\frac{\partial T}{\partial r} + w\frac{\partial T}{\partial z} + \lambda_2\left[u^2\frac{\partial^2 T}{\partial r^2} + w^2\frac{\partial^2 T}{\partial z^2} + \left(u\frac{\partial T}{\partial r} + w\frac{\partial u}{\partial z}\right)\frac{\partial T}{\partial z} + 2uw\frac{\partial^2 T}{\partial r\partial z}\right] =$$

$$= \alpha_{thnf}\frac{\partial^2 T}{\partial z^2} + \frac{\mu_{thnf}}{(\rho C_p)_{thnf}}\left(\frac{\partial u}{\partial z}\right)^2 + \frac{\sigma_{thnf}B^2u^2}{(\rho C_p)_{thnf}}. \tag{2.3}$$

The last term in Eq (2.2) represents Darcy resistance due to the porous medium, where k^* is the permeability. In this formulation, the effect of porosity is incorporated implicitly through the permeability parameter rather than appearing explicitly in the continuity equation. The porous medium is modeled under the local thermal equilibrium assumption, whereby the fluid and solid phases are assumed to share a common temperature due to rapid interfacial heat exchange and the thin surface-layer nature of the porous sheet. The above equations have to be solved subject to the boundary conditions:

$$\text{At } z = 0: \qquad u = U_w(r,t) + J_1\frac{\partial u}{\partial z}, \qquad w = 0, \qquad -k_f\frac{\partial T}{\partial z} = h_S(T_w - T), \tag{2.4}$$

$$\text{As } z \to \infty: \qquad u \to 0, \qquad T \to T_\infty, \tag{2.5}$$

where J_1 is the velocity slip coefficient and h_S is the surface heat transfer coefficient.

The magnetic dissipation term in the energy equation represents Joule (ohmic) heating, $q_J \sim \sigma_{thnf}B_0^2U^2$, generated by electric currents induced by the motion of the conducting nanofluid in the applied magnetic field. A simple scaling shows that its importance relative to conduction is $q_J/q_{cond} \sim Ha^2Br$. while its magnitude relative to viscous dissipation is $q_J/q_{visc} \sim Ha^2$, where $Ha = B_0L\sigma_{thnf}/\mu_{thnf}$ is the Hartmann number and $Br = \mu_{thnf}U^2/(k_{thnf}\Delta T)$ is the Brinkman number. Thus, Joule heating becomes comparable to other thermal effects when $Ha^2Br = O(1)$ (or, equivalently, when the coefficient multiplying the Joule term in the non dimensional energy equation is $O(1)$), otherwise it acts as a higher-order correction. This scaling clarifies that magnetic dissipation

is most significant for sufficiently strong magnetic fields and/or enhanced electrical conductivity of the ternary hybrid nanofluid. In these relations, U is a characteristic velocity and $\Delta T = T_w - T_\infty$. Therefore, although convective transport remains dominant, magnetic dissipation contributes significantly to near-wall thermal energy accumulation and entropy generation. Therefore, neglecting magnetic dissipation would underestimate thermal irreversibility in the MHD-assisted ternary hybrid nanofluid system.

To simplify the governing equations, we introduce similarity transformations. These transformations reduce the partial differential equations into a system of coupled, nonlinear ordinary differential equations by combining the spatial and temporal variables into a single similarity variable. A stream function formulation is employed to automatically satisfy the continuity equation, and the dimensionless temperature is defined relative to the surface and ambient temperatures.

For the unsteady radial stretching velocity

$$U_w(r,t) = \frac{br}{1-ct}, \tag{2.6}$$

we define the similarity variable and dimensionless temperature as

$$\eta = z\sqrt{\frac{b}{\nu_f(1-ct)}}, \qquad \theta(\eta) = \frac{T-T_\infty}{T_w-T_\infty}. \tag{2.7}$$

(Notice that with $Re = \dfrac{rU_w}{\nu_f} = \dfrac{br^2}{\nu_f(1-ct)}$, the definition $\eta = z\sqrt{\dfrac{b}{\nu_f(1-ct)}}$ is equivalent to $\eta = \dfrac{z}{r}\sqrt{Re}$.)

The Stokes stream function is introduced as

$$\Psi(r,z,t) = -r^2 U_w(r,t)\sqrt{\frac{\nu_f(1-ct)}{b}}\, f(\eta), \tag{2.8}$$

so that the continuity equation is satisfied identically via

$$u = \frac{1}{r}\frac{\partial \Psi}{\partial z}, \qquad w = -\frac{1}{r}\frac{\partial \Psi}{\partial r}. \tag{2.9}$$

Using Eqs (2.7)–(2.9), the velocity components become

$$u = \frac{br}{1-ct} f'(\eta), \qquad w = -2\sqrt{\frac{b\nu_f}{1-ct}}\, f(\eta), \tag{2.10}$$

where a prime denotes differentiation with respect to η.

Let us now rewrite the dimensional boundary conditions given by Eqs (2.4) and (2.5). From Eq (2.10), the no-penetration condition $w(0) = 0$ gives

$$f(0) = 0. \tag{2.11}$$

For the slip condition, we compute

$$\frac{\partial u}{\partial z} = \frac{br}{1-ct} f''(\eta)\frac{\partial \eta}{\partial z} = \frac{br}{1-ct} f''(\eta)\sqrt{\frac{b}{\nu_f(1-ct)}}. \tag{2.12}$$

Substituting into Eq (2.5) and dividing by $U_w = \dfrac{br}{1-ct}$ yields

$$f'(0) = 1 + S_n f''(0), \qquad S_n = J_1 \sqrt{\frac{b}{\nu_f(1-ct)}}. \tag{2.13}$$

where S_n is the slip parameter. For the convective thermal boundary condition, we note that

$$\frac{\partial T}{\partial z} = (T_w - T_\infty)\theta'(\eta)\frac{\partial \eta}{\partial z} = (T_w - T_\infty)\theta'(\eta)\sqrt{\frac{b}{\nu_f(1-ct)}}. \tag{2.14}$$

Substituting into (2.5) gives

$$-\theta'(0) = B_t(1-\theta(0)), \qquad B_t = \frac{h_S}{k_f}\sqrt{\frac{\nu_f(1-ct)}{b}}, \tag{2.15}$$

where B_t is the Biot number associated with the convective surface heating.

Finally, the far-field conditions (2.5) reduce to

$$f'(\eta) \to 0, \qquad \theta(\eta) \to 0 \quad \text{as} \quad \eta \to \infty. \tag{2.16}$$

These transformed boundary conditions, together with the reduced similarity equations, constitute a closed nonlinear boundary-value problem, which is solved numerically to analyze the effects of the governing parameters on the velocity, temperature, skin-friction coefficient, Nusselt number, and entropy generation rate.

Next, we use the similarity transformation to simplify Eqs (2.2) and (2.3) to the dimensionless Navier-Stokes and energy equations that now take the form

$$f''' - \frac{\delta_4}{\delta_1}Mf' - \frac{\delta_3}{\delta_1}P_K f' - \frac{\delta_3}{\delta_1}S_P\left(\frac{\eta}{2}f'' + f'\right) - \frac{\delta_3}{\delta_1}(f')^2 + 2\frac{\delta_3}{\delta_1}ff' = 0 \tag{2.17}$$

$$\left(\frac{\delta_2}{\delta_5 P_r} - 4\mathcal{D}f^2\right)\theta'' + \left[S_p\left(2\theta + \frac{\eta}{2}\theta'\right) + 2f'\theta - 2f\theta'\right] - 2D\left[\theta(f')^2 - 2ff'\theta' - 2ff''\theta\right] + \\ + \frac{\delta_1}{\delta_5}E_t(f'')^2 + \frac{\delta_4}{\delta_5}ME_t(f')^2 = 0, \tag{2.18}$$

where we introduced the quantities

$$\delta_1 = \frac{\mu_{thnf}}{\mu_f}, \quad \delta_2 = \frac{k_{thnf}}{k_f}, \quad \delta_3 = \frac{(\rho\beta)_{thnf}}{(\rho\beta)_f}, \quad \delta_4 = \frac{\sigma_{thnf}}{\sigma_f}, \quad \delta_5 = \frac{(\rho C_P)_{thnf}}{(\rho C_P)_f}$$

and we used the standard dimensionless quantities defined as

$$\text{Prandl number: } P_r = \frac{\rho C_p \nu_f}{k_f}; \quad \text{Porosity parameter: } P_S = \frac{\mu_f}{\rho_f K^*};$$

$$\text{Magnetic parameter: } M = \frac{\sigma_f B_0^2}{b\rho_f}; \quad \text{Eckert number: } E_t = \frac{b\nu_f}{c_P T_r};$$

$$\text{Unsteadiness parameter: } S_p = \frac{c}{b}; \quad \text{Relaxation parameter: } D = \lambda^* b^2.$$

These equations are solved numerically to analyze the effects of various physical parameters on the velocity, temperature, skin friction coefficient, Nusselt number, and entropy generation rate.

3. Entropy generation

Entropy generation is crucial in heat transfer analysis and validating advanced MHD nanofluid systems, measuring irreversibility in thermodynamic processes. ternary hybrid nanofluids have a specific definition of entropy production. This quantity can be defined as

$$E_g = \frac{k_{thnf}}{T_\infty^2}\left(\frac{\partial T}{\partial z}\right)^2 + \frac{\mu_{thnf}}{T_\infty}\left(\frac{\partial u}{\partial z}\right)^2 + \frac{\sigma_{thnf}B_0^2}{T_\infty}u^2 + \frac{\mu_{thnf}}{T_\infty k^*}. \tag{3.1}$$

The entropy generation number (N_g) has been determined as $N_g = E_g/E_0$ or, in other words, as

$$N_g = \delta_2 Re\theta'^2 + \delta_4\frac{MBr}{Re}f'^2 + \delta_1\frac{BrRe}{A}\left(\frac{f'^2}{P_S} + f''^2\right), \tag{3.2}$$

where we used [15]

$$E_0 = \frac{k_f(T_w - T_\infty)^2}{b^2T_\infty^2}, \quad A = \frac{\delta T}{T_\infty}.$$

We should note here that for simplicity we have considered that the difference between the wall and the far-field temperature are small, therefore the expression of the temperature in the expression of entropy will be approximated by T_∞

4. Characteristics of ternary hybrid nanoparticles

Details of the characteristics of ternary hybrid nanoparticles are given in Table 1, while Table 2 displays the nanoparticle shape factor for various nanoshapes. In addition, the physical properties of three different types of THN and base fluids are given as [16]

- Dynamic viscosity:

$$\mu_{thnf} = (1 + s_0\varphi_1 + s_1\varphi_1^2)(1 + s)(\varphi_2 + s_1\varphi_2^2)(1 + s_0\varphi_3 + s_1\varphi_3^2).$$

- Density:

$$\rho_{thnf} = (1 - \phi_3)\Big((1 - \phi_2)\Big[(1 - \phi_1)\rho_f + \phi_1\rho_{p1}\Big] + \phi_2\rho_{p2}\Big) + \phi_3\rho_{p3}.$$

- Electrical conductivity:

$$\sigma_{thnf} = \sigma hnf\frac{\sigma_3 + (p-1)\sigma_{hnf} - (p-1)\varphi_3(\sigma_{hnf} - \sigma_3)}{\sigma_3 + (p-1)\sigma_{hnf} + \varphi_3(\sigma_{hnf} - \sigma_3)},$$

with

$$\sigma_{hnf} = \sigma_{nf}\frac{\sigma_2 + (p-1)\sigma_{nf} - (p-1)\varphi_2(\sigma_{nf} - \sigma_2)}{\sigma_2 + (p-1)\sigma_{nf} + \varphi_2(\sigma_{nf} - \sigma_2)},$$

and

$$\sigma_{nf} = \sigma_f\frac{\sigma_1 + (p-1)\sigma_f - (p-1)\varphi_1(\sigma_f - \sigma_1)}{\sigma_1 + (p-1)\sigma_f + \varphi_1(\sigma_f - \sigma_1)}.$$

- Thermal conductivity:

$$k_{thnf} = k_{hnf}\frac{k_3 + (p-1)k_{hnf} - (p-1)\varphi_3(k_{hnf} - k_3)}{k_3 + (p-1)k_{hnf} + \varphi_3(k_{hnf} - k_3)},$$

where

$$k_{hnf} = k_{nf}\frac{k_2 + (p-1)k_{nf} - (p-1)\varphi_2(k_{nf} - k_2)}{k_2 + (p-1)k_{nf} + \varphi_2(k_{nf} - k_2)},$$

and

$$k_{nf} = k_f\frac{k_1 + (p-1)k_f - (p-1)\varphi_1(k_f - k_1)}{k_1 + (p-1)k_f + \varphi_1(k_f - k_1)}.$$

- Heat capacity:

$$(\rho c_p)_{thnf} = (1 - \varphi_2 - \varphi_3 + \varphi_2\varphi_3)\Big[(1-\varphi_1)(\rho c_p)_f + \varphi_1(\rho c_p)_1\Big] + (1-\varphi_3)\varphi_2(\rho c_p)_2 + \varphi_3(\rho c_p)_3.$$

- Coefficient of thermal expansion

$$(\rho\beta)_{thnf} = (1-\varphi_3)\Big((1-\varphi)\Big[(1-\varphi_1)(\rho\beta)_f + \varphi_1(\rho\beta)_1\Big] + \varphi_2(\rho\beta)_2\Big) + \varphi_3(\rho\beta)_3.$$

Table 1. Thermophysical properties of liquid-based nanomaterials where, the base fluid is the H_2O/EG mixture

Material	ρ (kg/m^3)	C_p (J/kg·K)	k (W/m·K)	σ (S/m)	β (K^{-1})	Pr
Base fluid	1063.8	3630	0.387	9.75×10^{-4}	5.8×10^{-4}	29.86
Cu	8933	385	401	5.96×10^{7}	1.67×10^{-4}	–
MoS_2	5060	397.21	904.4	2.09×10^{4}	2.84×10^{-5}	–
GO	1800	717	5000	6.30×10^{7}	2.84×10^{-4}	–

Table 2. The shape factor for different nanoparticle geometries [16, 17].

Nanoparticle geometry	s_0	s_1	p
Blade –shaped	14.6	123.3	8.26
Brick–shaped (cuboid)	1.9	471.4	3.72
Cylindrical (rod–like)	13.5	904.4	4.82

5. Numerical solution procedure

The reduced system of coupled nonlinear ordinary differential equations (Eqs 2.17 and 2.18), together with the boundary conditions at $\eta = 0$ and $\eta \to \infty$, constitutes a two-point boundary value problem. This system is solved numerically using a shooting method combined with a classical fourth-order Runge–Kutta integration scheme.

In the shooting approach, the boundary value problem is first transformed into an equivalent initial value problem by introducing appropriate guesses for the unknown initial conditions (such as $f''(0)$ and $\theta(0)$. These guesses are iteratively refined using a Newton-type correction procedure until the far-field boundary conditions $f'(\eta) \to 0$ and $\theta(\eta) \to 0$ are satisfied within a prescribed tolerance.

Since the boundary conditions are specified at infinity, the computational domain is truncated at a finite value η_{max}. After several numerical experiments, $\eta_{max} = 8$ was found sufficient to ensure that the asymptotic conditions are satisfied with residual errors less than 10^{-8}. Increasing the maximum value of η beyond this point produced no significant change in the computed physical quantities. The integration was performed with a uniform step size $h = 0.01$. Convergence of the solution was confirmed by reducing the step size and verifying that variations in key parameters, such as the skin friction coefficient and Nusselt number, remain below 10^{-6}, confirming grid independence and numerical stability of the obtained solutions.

6. Solution methodology

The network diagram (Figure 2) represents an artificial neural network (ANN) architecture for modelling the entropy generation analysis of MHD flow and heat transfer of $(Cu\text{-}MoS_2\text{-}GO/EG - H_2O)$ over an expanding porous sheet. The feedforward ANN model consists of four layers: an input layer, hidden layers 1 and 2 for feature processing, and an output layer. Each layer contains two fundamental elements: weight (W) and bias (b). The network follows a feedforward architecture, with input data flowing from left to right, weights multiplying input values, summation operations combining weighted inputs and biases, and activation functions transforming summed values into neuron outputs.

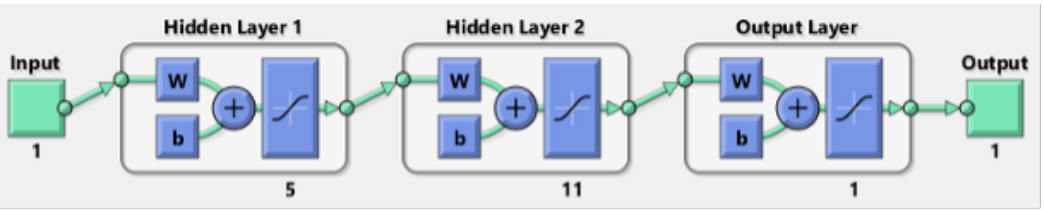

Figure 2. Schematic diagram of ANN model.

The methodological workflow is shown in Figure 3. Panel (a) demonstrates a neural network learning process with proper convergence features, meaning that the model will have learnd from the training data and achieved the best performance by the end of the 116-epoch training period. Panel (b) displays a validation performance comparison of different models, resulting in a great change in mean squared error (MSE) above 110 epochs with a performance of 2.1217×10^{-7}. The error histogram shown in panel (c) describes the prediction errors that are spread out among the training, validation, test, and merged datasets using 20 bins. Finally, Panel (d) shows a machine learning model that was successfully trained and is ready for use in the real world. This model has strong predictive performance, high R-values, and tight linear clustering. The proposed ANN serves as a surrogate model that eliminates the need for repeated numerical integration, enables rapid evaluation across a wide multidimensional parameter space, and it is suitable for real-time engineering estimation and parametric optimization studies. Thus, the ANN employed in our study transforms the computationally intensive boundary value problem into a fast predictive tool.

We emphasize that the simplicity of our ANN, with complex interactions among Hartmann number, nanoparticle volume fraction and shape factors as inputs and the solution (i.e. velocity profiles, temperature distributions, skin friction coefficient, Nusselt number, and entropy generation)

as output, was intentional, as it allows reliable predictions with minimal computational cost while maintaining high accuracy. Despite the small network size, it effectively captures the nonlinear relationship between process variables, demonstrating that even a compact ANN can be sufficient for modeling MHD boundary-layer flow.

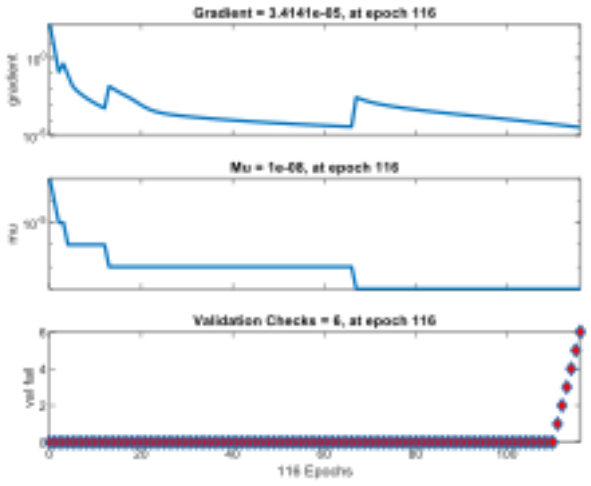

(a) Convergence characteristics of the neural network.

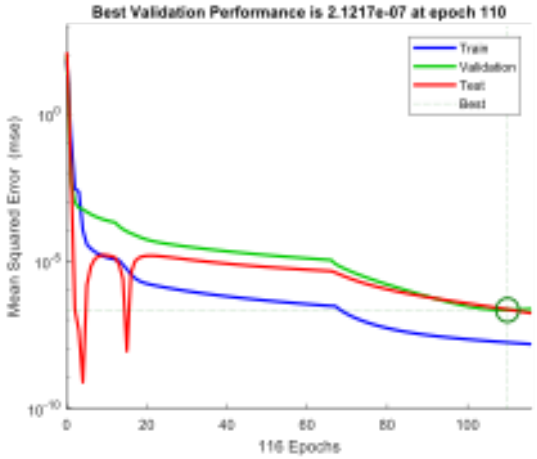

(b) Validation performance comparison.

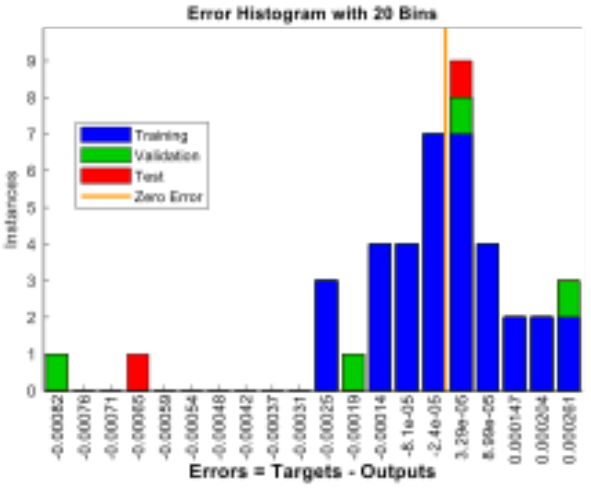

(c) Error distribution.

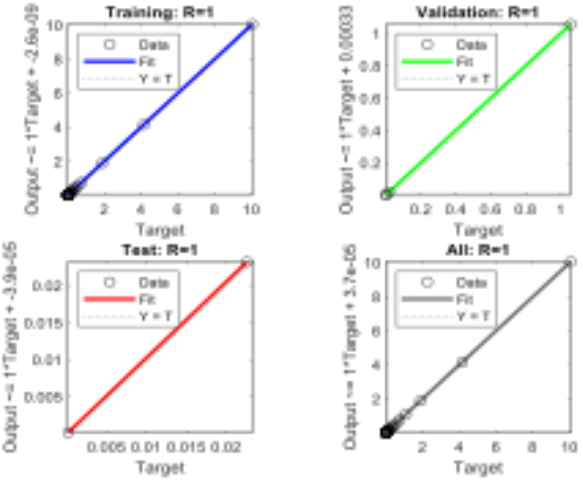

(d) *R*-values.

Figure 3. (a) Here we show the outcomes of our ANN approach. (a) Training state, (b) performance, (c) error histogram, and (d) regression.

7. Validation of results

Figure 4(a) shows a neural network performance evaluation scatter plot comparison showing target vs. predicted values. This figure confirms that this neural network model has achieved excellent predictive performance with a strong correlation between predicted and actual values across all dataset

splits. The current results in Tables 4 and 5 demonstrate strong agreement with previous results [16, 18–20], validating the model's reliability and justifying its further application.

Table 3. Comparison of current results with earlier results [18] for $\hat{C}_f$

S	M	K	φ	**Reference [18]**		**ANN**	
				Blade	Cylinder	Blade	Cylinder
0.8	1.0	0.5	0.04	−1.3806372	−2.0028919	−1.3806371	−2.0028987
0.8	1.0	0.5	0.03	−1.1466836	−0.97327714	−1.1466834	−0.97327717
1.2	1.0	1.0	0.04	−1.2979466	−1.8887102	−1.2979465	−1.88871008
1.2	1.0	0.5	0.03	−1.1466836	−0.97327714	−1.1466837	−0.97327712

Table 4. Comparison of current results with earlier results [16, 18–20] for $f''(0)$

S	β	**[19]**	**[16]**	**[20]**	**[18]**	**Present study**
0.4	4.981455	−1.134098	−1.134	−1.134096	-1.134096	−1.134097
0.6	3.131710	−1.195128	−1.195	−1.195125	-1.195125	−1.195126
0.8	2.151990	−1.245805	−1.246	−1.245806	-1.245805	−1.2458042

Table 5. Comparison of current results for $f''(0)$

S	β	**Present**		**Error**
		Numerical	**ANNs**	
0.4	4.981455	−1.13409724782	−1.13409724689	9.3×10^{-10}
0.6	3.131710	−1.19512607935	−1.19512607894	4.1×10^{-10}
0.8	2.151990	−1.24580425368	−1.24580425198	1.7×10^{-9}

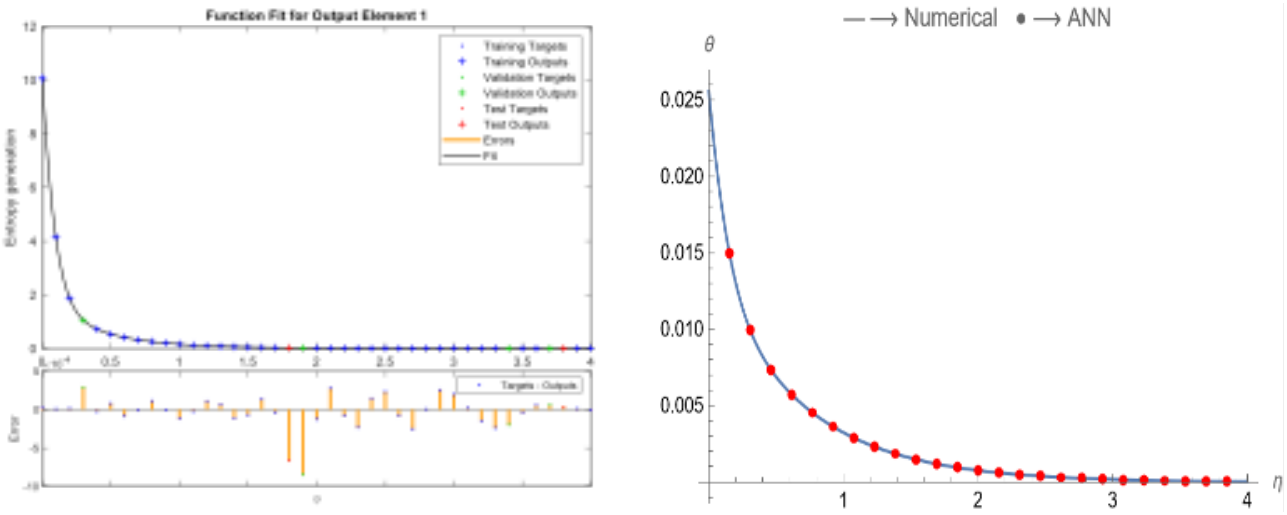

(a) $N_g(\eta)$ **(b)** $\theta(\eta)$.

Figure 4. Comparison of ANN results with results generated by our numerical analysis.

8. Results and discussion

8.1. Ternary hybrid nanofluid flow

Figure 5 presents the effect of the magnetic parameter, M, on the f' profile. The magnetic field creates a body force that opposes fluid motion, effectively thickening the momentum boundary layer and reducing the overall velocity magnitude. This is typical behavior in MHD flow problems where the magnetic parameter M is the ratio of magnetic forces to viscous forces.

As shown in Figure 6, increasing the unsteadiness parameter S_p (from 0.0 to 0.2) results in a uniform decline in the velocity gradient f' within the boundary layer. This trend confirms that unsteadiness effects associated with temporal acceleration/deceleration act to diminish the velocity distribution.

As shown in Figure 7, progressively increasing the slip parameter S_n from 0 and 1.2 leads to a pronounced decline in the dimensionless velocity f' across the boundary layer. The maximum velocity is obtained under the classical no-slip condition ($S_n = 0$), whereas the greatest slip ($S_n = 1.2$) yields the weakest velocity response. This behaviour reflects the fact that increasing slip reduces the frictional resistance at the wall, thereby diminishing the transfer of momentum from the surface to the fluid and weakening the velocity development in the boundary layer.

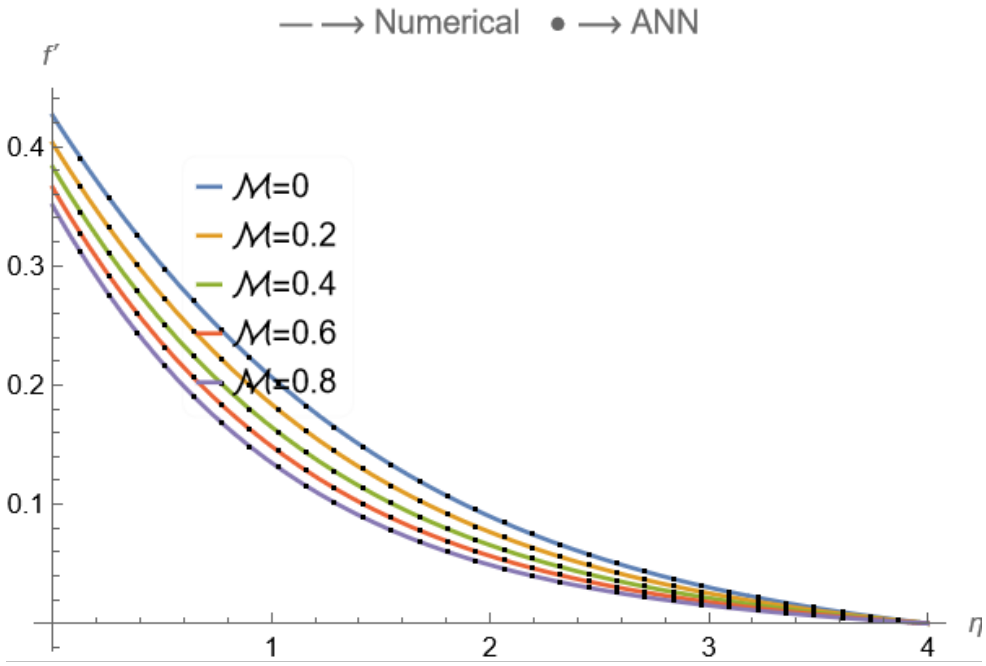

Figure 5. The influence of the magnetic parameter, M, on the dimensionless velocity profile f'. Increasing M enhances the Lorentz force, which suppresses fluid motion and thickens the momentum boundary layer. Here (and in all subsequent plots), the dashed lines denote numerical results, while solid lines stand for the results obtained using an ANN approach.

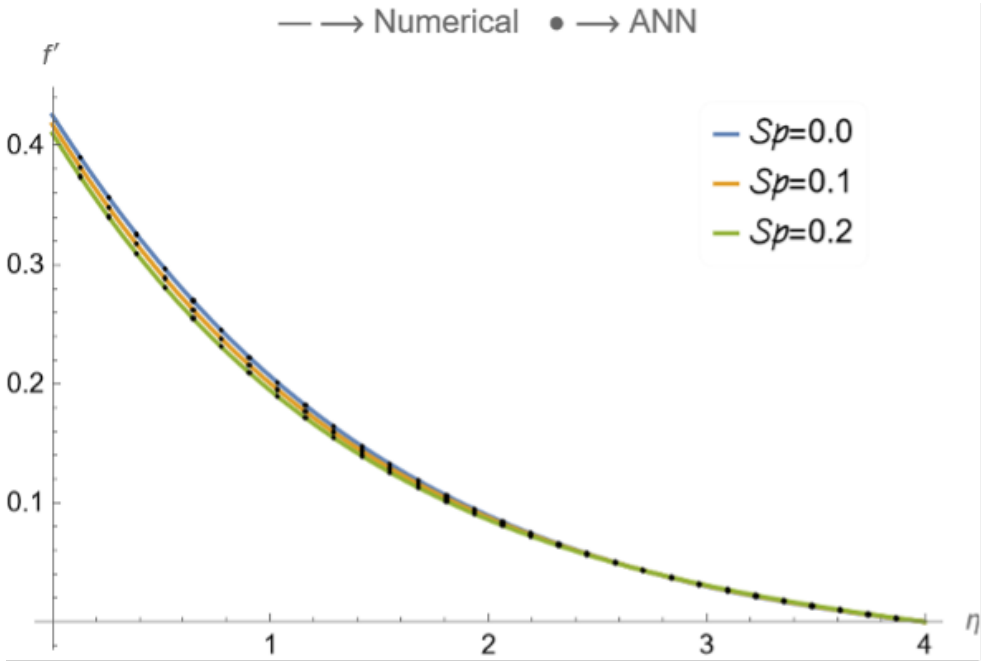

Figure 6. Variation of the dimensionless velocity profile $f'(\eta)$ for different values of the unsteadiness parameter S_p. Temporal acceleration effects modify the boundary-layer structure and reduce the peak velocity.

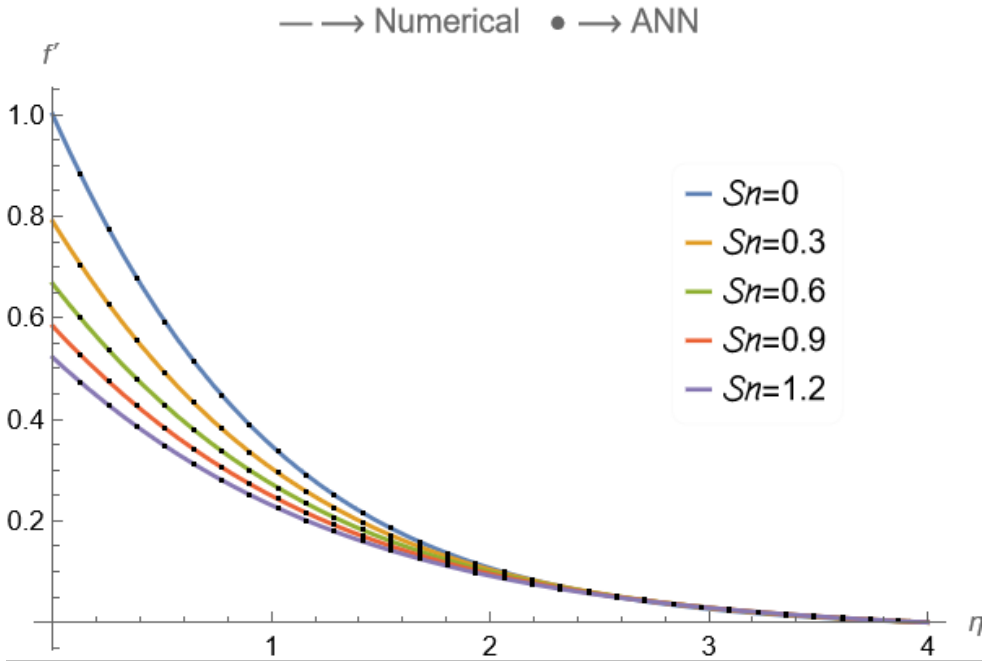

Figure 7. Effect of the velocity slip parameter S_n on the velocity distribution f'. Increasing wall slip weakens shear transmission from the surface and reduces near-wall momentum.

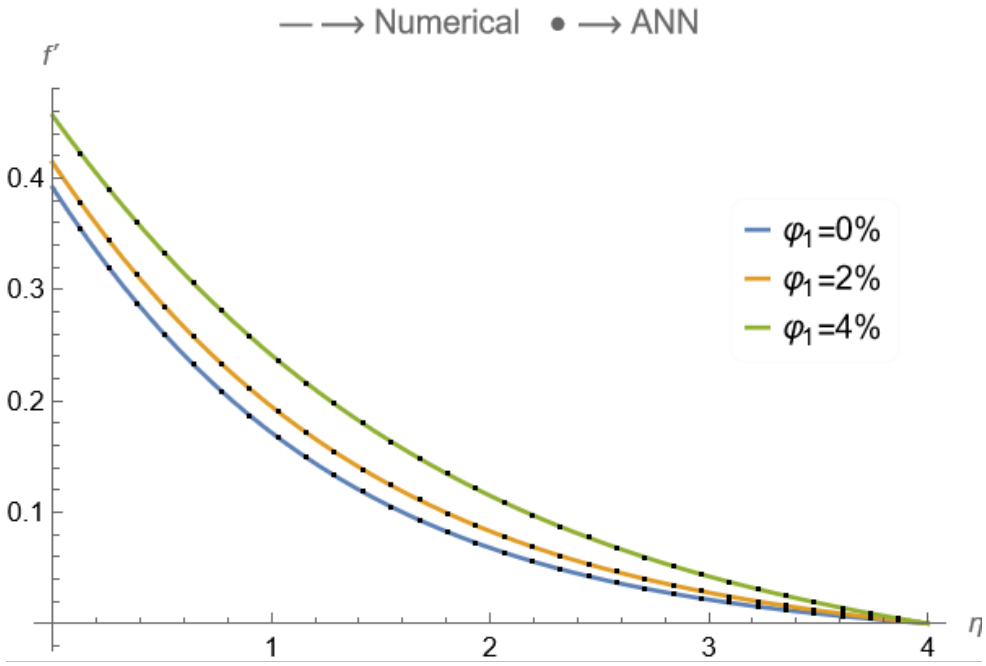

Figure 8. The influence of nanoparticle volume fraction φ_1 on the dimensionless velocity profile f'. It is clear that increasing particle concentration enhances the velocity distribution within the boundary layer.

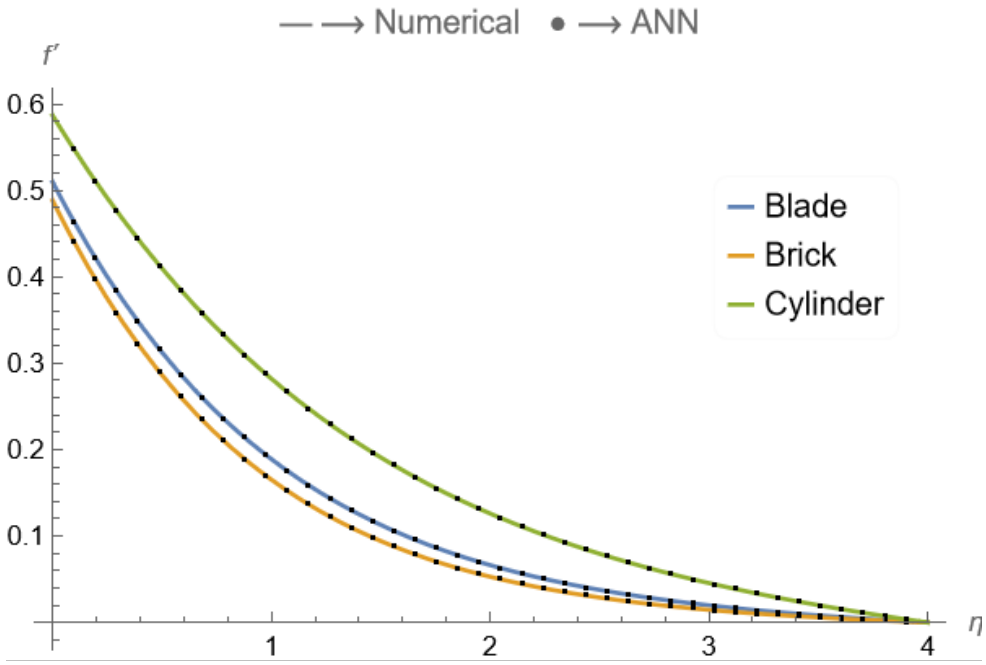

Figure 9. The influence of nanoparticle shape factor, p, (blade, brick, and cylinder) on the dimensionless velocity profile $f'(\eta)$. Variations in particle geometry modify the momentum boundary-layer structure and alter the velocity decay within the flow.

Figure 8 illustrates the effect of nanoparticle volume fraction φ_1 on the velocity profile f'. As

φ_1 increases from 0% to 4%, the dimensionless velocity rises throughout the boundary layer. The pure base fluid exhibits the lowest velocity profile, while the highest concentration corresponds to the maximum velocity.

Figure 9 illustrates the influence of nanoparticle shape, p (blade, brick, and cylinder) on the velocity profile f'. As the particle geometry becomes more streamlined, the momentum boundary-layer thickness decreases, indicating a faster decay of velocity away from the wall. These results demonstrate that particle morphology significantly influences the momentum transport characteristics of the boundary layer.

8.2. Heat transfer profile

Figure 10 highlights that the magnetic parameter M is changing the profile of $\theta(\eta)$. The consequence of increasing the magnetic field is creating a Lorentz force that works as a resistive drag against fluid motion. This retards the fluid velocity, resulting in decreased convective cooling and causing more heat to accumulate near the wall. The thermal boundary layer thickens, and temperature gradients decrease.

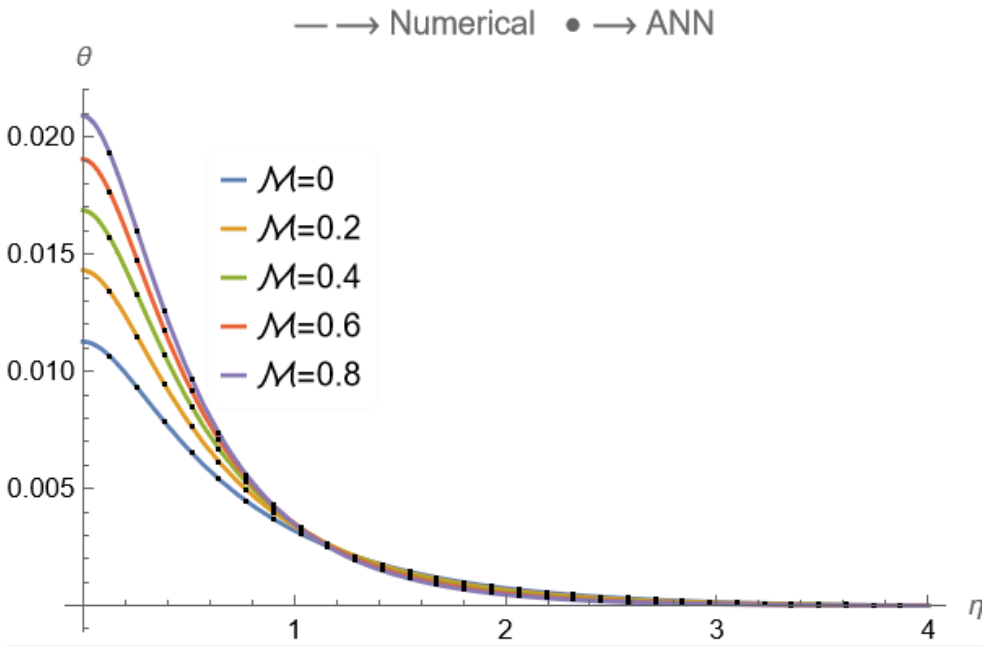

Figure 10. The effect of the magnetic value M on the temperature distribution $\theta(\eta)$). Clearly, increasing M suppresses convective transport due to the Lorentz force, resulting in a thicker thermal boundary layer and elevated temperatures near the wall.

Figure 11 describes the consequences of the unsteadiness factor S_p on the $\theta(\eta)$ profile. As the unsteadiness parameter S_p increases, the flow adjusts more rapidly to temporal variations, resulting in heightened rates of heat dissipation and enhanced transient cooling. This results in a reduction of the thermal boundary layer thickness, enabling a more significant temperature gradient from the wall to the fluid, hence diminishing the overall profile of $\theta(\eta)$.

Figure 12 displays the impact of slip value S_n on the profile of $\theta(\eta)$. As the slip develops, the fluid velocity near the wall escalates, diminishing the capacity of the fluid to store heat adjacent to the surface. This improves convective heat transfer, facilitating more rapid heat dissipation from the wall

to the fluid, resulting in a smaller thermal boundary layer and a reduced overall $\theta(\eta)$ profile.

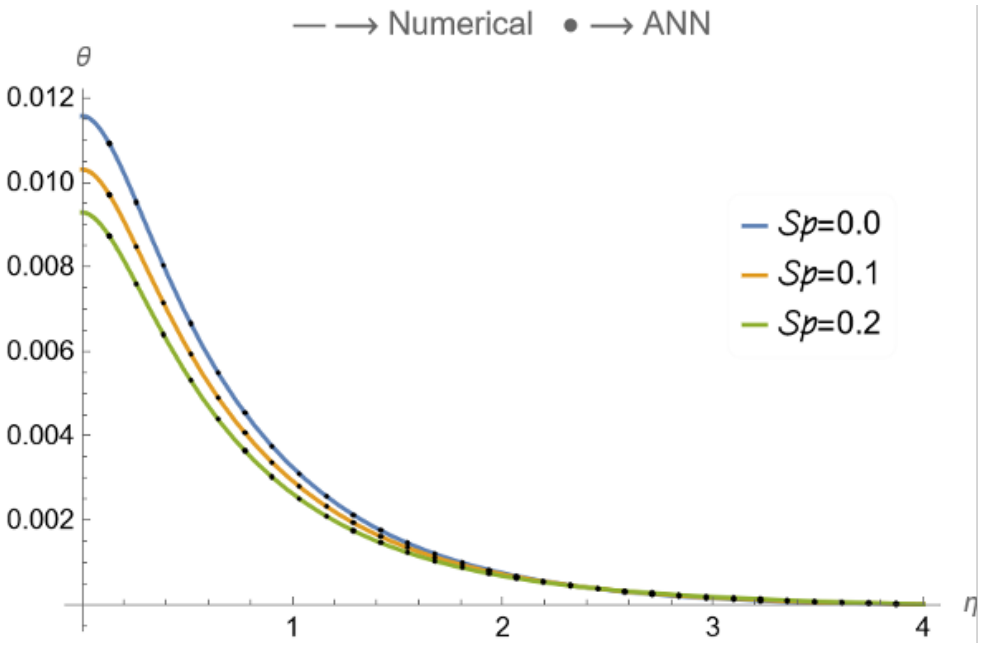

Figure 11. The influence of the unsteadiness parameter S_p on the profile of $\theta(\eta)$. Increasing S_p reduces the thermal boundary-layer thickness and lowers the temperature profile due to enhanced transient effects.

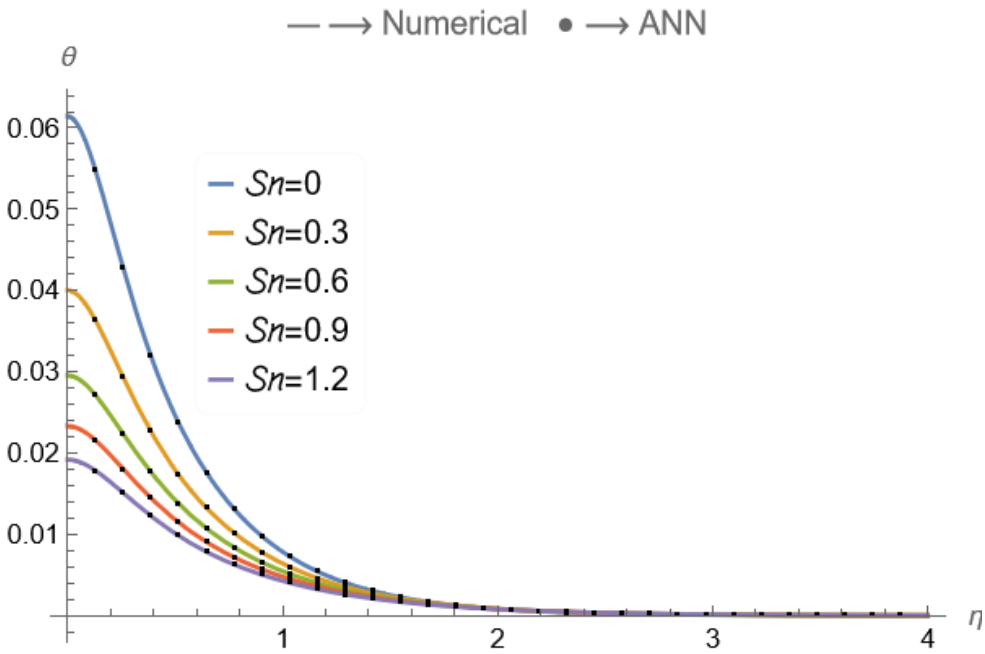

Figure 12. The effect of the slip parameter S_n on the profile of $\theta(\eta)$. Increasing wall slip enhances convective heat transport and reduces the thermal boundary-layer thickness.

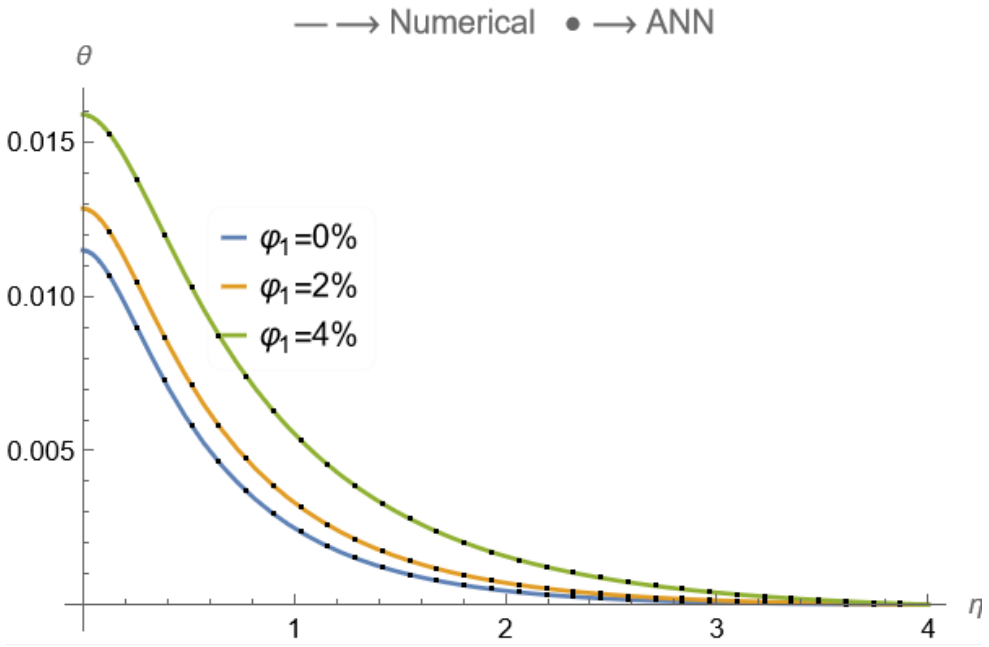

Figure 13. The influence of nanoparticle volume fraction φ_1 on profile of $\theta(\eta)$. Increasing φ_1 enhances effective thermal conductivity, resulting in higher boundary-layer temperatures.

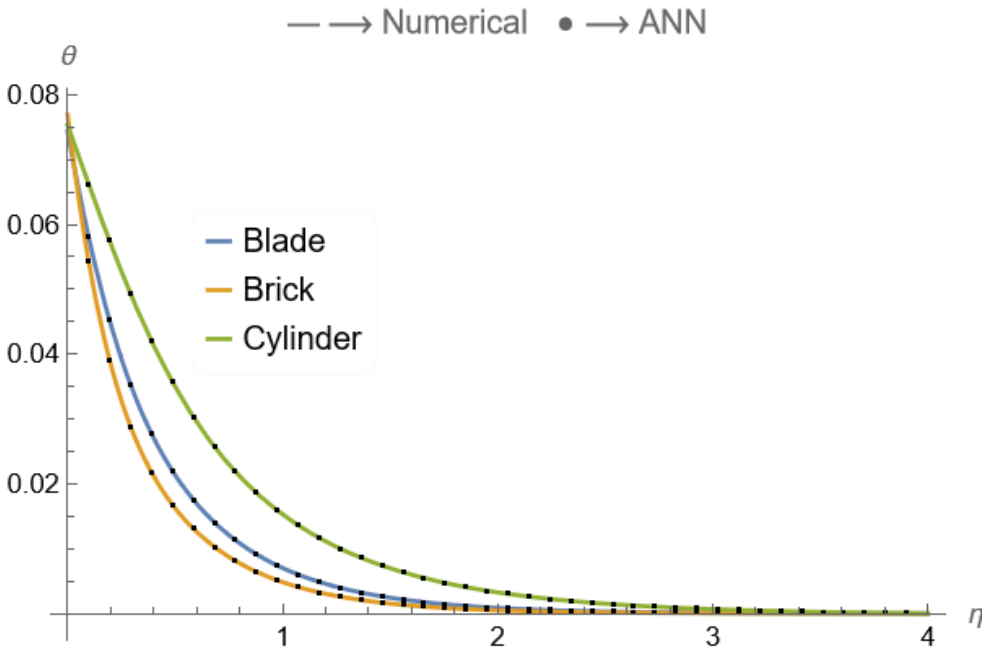

Figure 14. The effect of nanoparticle shape (blade, brick, and cylinder) on the dimensionless temperature profile, $\theta(\eta)$. Variations in particle geometry modify heat conduction and convection characteristics within the boundary layer.

Figure 13 examines the effect of nanoparticle volume fraction φ_1 on the profile of $\theta(\eta)$. A higher concentration of nanoparticles φ_1 enhances the absorption and dispersion of thermal energy within the boundary layer, leading in an elevated $\theta(\eta)$ profile. This indicates that heat is carried more efficiently

through the fluid, resulting in elevated temperatures near the wall due to enhanced energy transport.

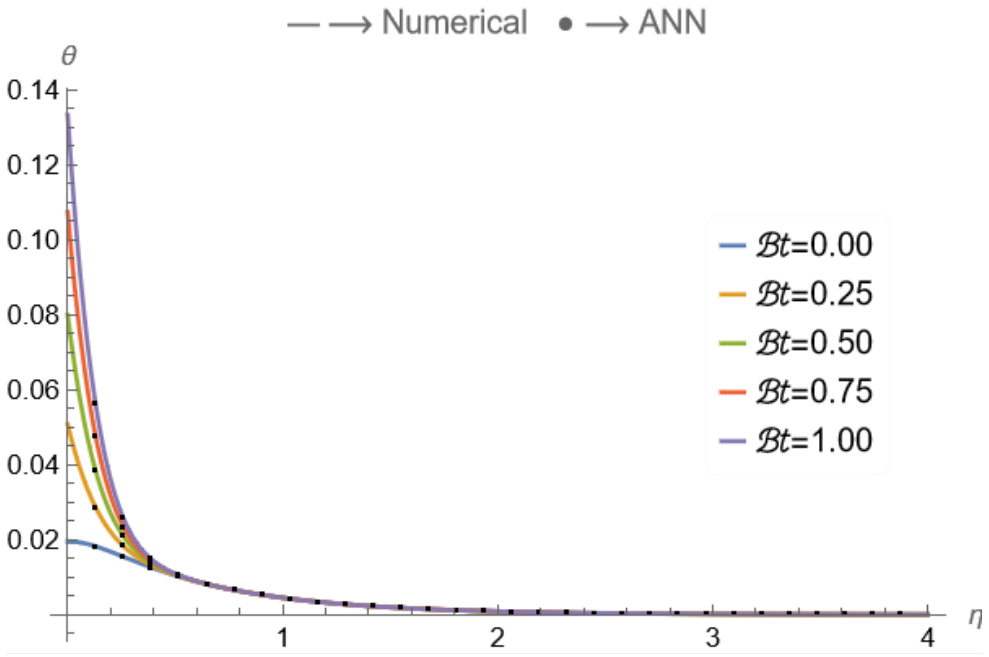

Figure 15. The effect of the Biot number, B_t, on the dimensionless temperature distribution. These results indicate that increasing B_t intensifies convective heat transfer at the surface, leading to steeper thermal gradients near the wall.

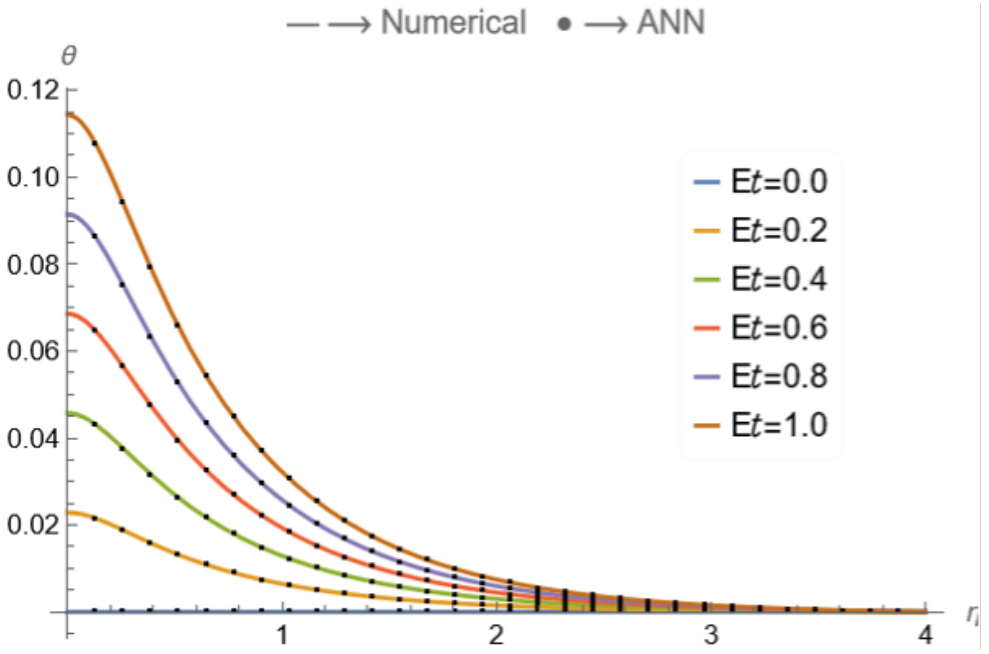

Figure 16. Influence of the Eckert number E_t on the temperature profile $\theta(\eta)$. Higher values of E_t enhance viscous dissipation, leading to increased thermal energy generation within the boundary layer.

Figure 14 shows the effect of shape factor (i.e. blade, brick, and cylinder) p on the profile of $\theta(\eta)$. The shape factor influences the rate of heat conduction and convection from the surface by modifying the flow structure and the features of the thermal boundary layer. More curved geometries, such as the cylinder, yield diminished cooling efficiency, holding heat for extended periods and generating a bigger thermal boundary layer with elevated temperature gradients away from the surface.

Figure 15 shows the impact of Biot number B_t on the profile of $\theta(\eta)$. In this figure, increasing the Biot number raises the $\theta(\eta)$ profile near the surface and increases the temperature gradient in the thermal boundary layer, which reflects faster heat exchange between solid and fluid.

In Figure 16, we display the impact of Eckert number, E_t, on the profile of $\theta(\eta)$. Increasing the Eckert number raises the temperature distribution in the boundary layer, and that means the viscous dissipation and the change of kinetic energy into thermal energy occur in thermal fluid systems.

8.3. Entropy generation

Figure 17 illustrates the consequences of the slip parameter S_n on the entropy generation profile. As the slip parameter S_n grows, momentum transfer near the wall and the associated viscous dissipation decrease, leading to a drop in entropy production. As mechanical and thermal irreversibilities fall, the N_g profile goes down, which means that the boundary layer is moving towards more reversible processes. Thus, increasing slip parameter S_n from 0 to 0.4 reduces peak entropy generation by approximately 19%, indicating a significant suppression of near-wall irreversibility

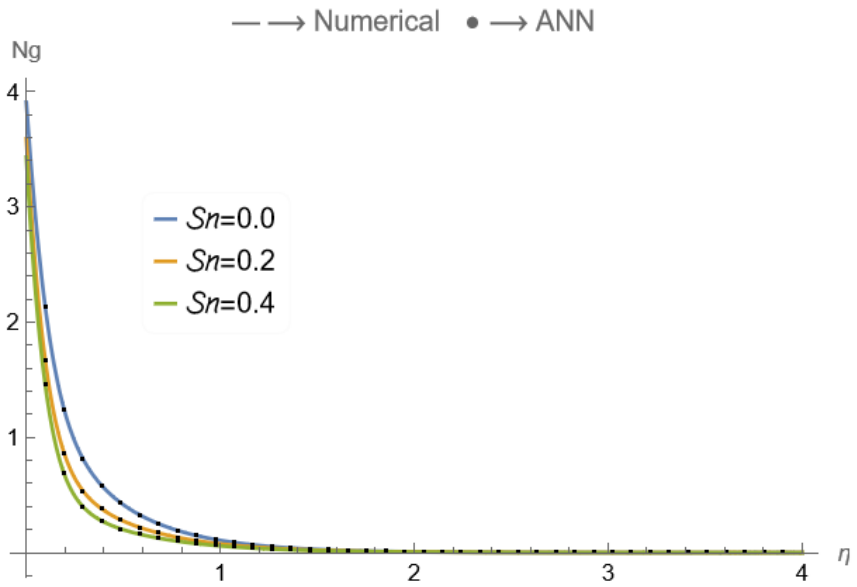

Figure 17. The effect of the velocity slip parameter S_n on the entropy generation profile $N_g(\eta)$. Increasing wall slip weakens near-wall momentum transfer and viscous dissipation, resulting in reduced thermodynamic irreversibility within the boundary layer.

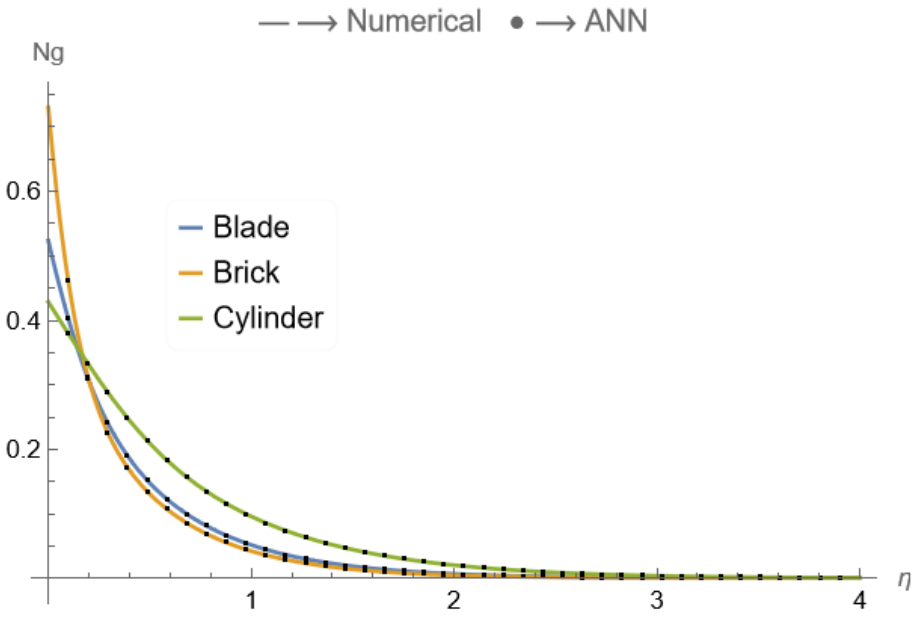

Figure 18. Influence of nanoparticle shape (blade, brick, and cylinder) on the profile of entropy generation, $N_g(\eta)$. Variations in particle geometry modify effective transport properties and alter irreversibility levels in the boundary layer.

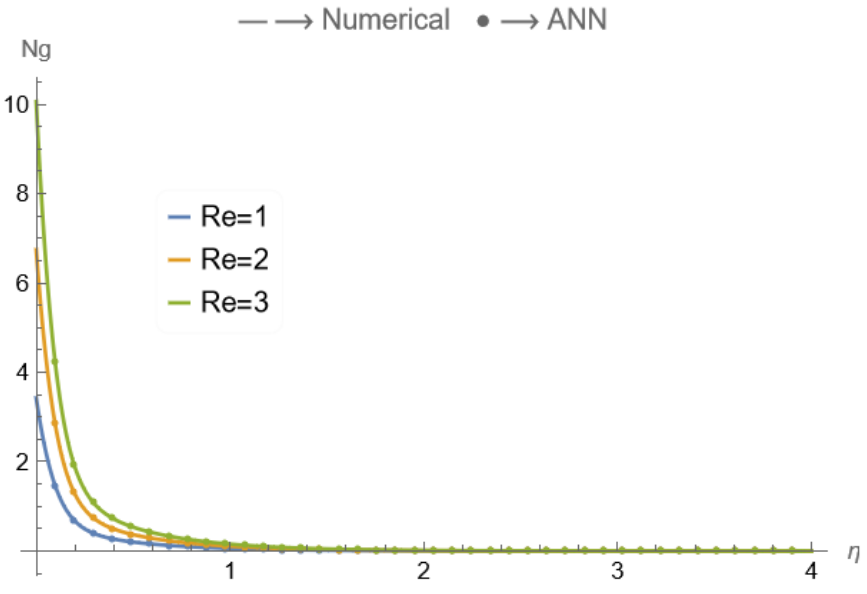

Figure 19. Influence of the Reynolds number *Re* on the dimensionless entropy generation profile $N_g(\eta)$. Higher Reynolds numbers intensify near-wall velocity and temperature gradients, leading to increased irreversibility in the boundary layer, while the effect becomes negligible farther from the surface.

Figure 18 displays the impact of shape factor (i.e., blade, brick, and cylinder) p on the entropy generation profile. Our analysis shows that the brick increases peak entropy by 34.6% and cylinder reduces entropy by 19.2%. Thus, changing from Blade to cylinder will increase the amount of entropy generated in the boundary layer, which suggests that shape is an important factor for improving thermodynamic efficiency and energy dissipation in thermal-fluid systems.

Figure 19 displays the effects of the Reynolds number, Re, on the entropy generation profile. Stronger gradients lead to increased irreversibilities due to both viscous dissipation and heat transfer, resulting in greater entropy generation. The effect diminishes farther from the wall, and the velocity and temperature gradients decrease, and, consequently, the effect of Re on N_g becomes negligible. Thus, increasing Reynolds number from 0 to 2, increases entropy gradient magnitude by approximately 188%, at least for small values of η. When $\eta \geq 1$, the entropy generation is small and is practically independent of the value of the Reynolds number.

9. Conclusions

In this study, we examined the unsteady magnetohydrodynamic boundary-layer flow of a $Cu - MoS_2 - GO$ ternary hybrid nanofluid over an expanding porous sheet, together with its heat transfer and entropy generation characteristics. The governing equations were reduced via similarity transformations and solved numerically, and a compact ANN surrogate model was developed for rapid prediction of key transport quantities.

From a transport perspective, the ternary hybrid nanofluid demonstrates enhanced thermal performance compared to conventional single or binary particle suspensions reported in the literature. The combined presence of copper (with high thermal conductivity), MoS_2 (lubrication and stability enhancement), and graphene oxide (large surface area and dispersion improvement) leads to stronger energy absorption and more effective heat redistribution within the boundary layer. This combination allows improved thermal control under magnetic and porous flow conditions, which may be advantageous in coating processes, membrane systems, and magnetically regulated cooling devices.

The magnetic field was shown to suppress fluid motion through Lorentz forces, thickening the momentum boundary layer and modifying thermal gradients. The unsteadiness parameter influences the temporal development of the boundary layer, while wall slip reduces shear stress and entropy production. Furthermore, particle morphology plays a non-negligible role: variations in nanoparticle shape alter effective transport properties and irreversibility levels, indicating that shape optimization may serve as a design parameter in advanced thermal-fluid systems.

From a thermodynamic viewpoint, the entropy analysis clarifies the relative contributions of heat-transfer irreversibility, viscous dissipation, magnetic effects, and porous resistance. This provides a quantitative basis for minimizing energy losses in magnetically controlled nanofluid flows. The ANN model further enhances practical applicability by enabling rapid parametric exploration without repeated numerical integration.

Despite these advantages, several limitations should be noted. The analysis is based on a similarity solution for an idealized axisymmetric expanding porous sheet, which represents circular stretching or membrane-type systems but does not directly describe rotating disks or fully three-dimensional geometries. The porous medium is modeled using Darcy resistance without Forchheimer inertia, and local thermal equilibrium is assumed. In addition, effective medium property models are employed,

which provide analytical consistency but may not capture all microscale particle interactions. Therefore, the present results are most applicable to laminar, moderate-temperature-difference regimes where these assumptions remain valid.

Use of Generative-AI tools declaration

The author declares they have not used Artificial Intelligence (AI) tools in the creation of this article.

Conflict of interest

The author of this manuscript have no conflicts of interest

References

1. S. U. S. Choi, Enhancing thermal conductivity of fluids with nanoparticles, *ASME international mechanical engineering congress and exposition*, **17421** (1995), 99–105. https://doi.org/10.1115/IMECE1995-0926
2. J. Buongiorno, Convective transport in nanofluids, *J. Heat Transfer.*, **128** (2006), 240–250. https://doi.org/10.1115/1.2150834
3. M. A. Sheremet, T. Groşan, I. Pop, Free convection in a square cavity filled with a porous medium saturated by nanofluid using Tiwari and Das' nanofluid model, *Transp. Porous. Med.*, **106** (2015), 595–610. https://doi.org/10.1007/s11242-014-0415-3
4. W. A. Khan, Z. H. Khan, M. Rahi, Fluid flow and heat transfer of carbon nanotubes along a flat plate with Navier slip boundary, *Appl. Nanosci.*, **4** (2014), 633–641. https://doi.org/10.1007/s13204-013-0242-9
5. T. Hayat, T. Muhammad, A. Alsaedi, M. S. Alhuthali, Magnetohydrodynamic three-dimensional flow of viscoelastic nanofluid in the presence of nonlinear thermal radiation, *J. Magn. Magn. Mater.*, **385** (2015), 222–229. https://doi.org/10.1016/j.jmmm.2015.02.046
6. M. M. Bhatti, A. Zeeshan, R. Ellahi, Entropy generation on MHD Eyring–Powell nanofluid through a permeable stretching surface, *Entropy*, **18** (2016), 224. https://doi.org/10.3390/e18060224
7. M. Ramzan, M. Bilal, J. D. Chung, Influence of homogeneous–heterogeneous reactions on MHD 3D Maxwell fluid flow with Cattaneo–Christov heat flux and convective boundary condition, *J. Mol. Liq.*, **230** (2017), 415–422. https://doi.org/10.1016/j.molliq.2017.01.061
8. M. Ghalambaz, E. Jamesahar, M. A. Ismael, A. J. Chamkha, Fluid-structure interaction study of natural convection heat transfer over a flexible oscillating fin in a square cavity, *Int. J. Therm. Sci.*, **111** (2017), 256–273. https://10.1016/j.ijthermalsci.2016.09.001
9. I. Tlili, N. N. Hamadneh, W. A. Khan, S. Atawneh, Thermodynamic analysis of MHD Couette–Poiseuille flow of water-based nanofluids in a rotating channel with radiation and Hall effects, *J. Therm. Anal. Calorim.*, **132** (2018), 1899–1912. https://doi.org/10.1007/S10973-018-7066-5
10. I. L. Animasaun, S. J. Yook, T. Muhammad, A. Mathew, Dynamics of ternary-hybrid nanofluid subject to magnetic flux density and heat source or sink on a convectively heated surface, *Surf. Interfaces*, **28** (2022), 101654. https://doi.org/10.1016/j.surfin.2021.101654

11. Z. Xuan, Y. Zhai, M. Ma, Y. Li, H. Wang, Thermo-economic performance and sensitivity analysis of ternary hybrid nanofluids, *J. Mol. Liq.*, **323** (2021), 114889. https://doi.org/10.1016/j.molliq.2020.114889

12. X. Yang, A. Boroomandpour, S. Wen, D. Toghraie, F. Soltani, Applying artificial neural networks (ANNs) for prediction of the thermal characteristics of water/ethylene glycol-based mono, binary and ternary nanofluids containing MWCNTs, titania, and zinc oxide, *Powder Technol.*, **388** (2021), 418–424. https://10.1016/j.csite.2021.101122

13. F. A. Shah, N. S. Akbar, T. Zamir, M. Abd El-Rahman, W. A. Khan, Thermal energy analysis using artificial neural network and particle swarm optimization approach in partially ionized hyperbolic tangent material with ternary hybrid nanomaterials, *Swarm Evol. Comput.*, **91** (2024), 101775. https://doi.org/10.1016/j.swevo.2024.101775

14. L. J. Crane, Flow past a stretching plate, *J. Appl. Math. Phys.*, **21** (1970), 645–647. https://doi.org/10.1007/BF01587695

15. H. Waqas, M. Fida, D. Liu, U. Manzoor, T. Muhammad, Numerical simulation of entropy generation for nanofluid with the consequences of thermal radiation and Cattaneo-Christov heat flux model, *Int. Commun. Heat Mass Transfer*, **137** (2022), 106293. https://doi.org/10.1016/j.icheatmasstransfer.2022.106293

16. S. Bibi, Z. Elahi, A. Shahzad, Impacts of different shapes of nanoparticles on SiO_2 nanofluid flow and heat transfer in a liquid film over a stretching sheet, *Phys. Scr.*, **95** (2020), 115217. https://doi.org/10.1088/1402-4896/abbc9d

17. Z. H. Khan, S. T. Hussain, Z. Hammouch, Flow and heat transfer analysis of water and ethylene glycol based Cu nanoparticles between two parallel disks with suction/injection effects, *J. Mol. Liq.*, **221** (2016), 298–304. https://doi.org/10.1016/j.molliq.2016.05.089

18. U. Hayat, R. Ali, S. Shaiq, A. Shahzad, A numerical study on thin film flow and heat transfer enhancement for copper nanoparticles dispersed in ethylene glycol, *Rev. Adv. Mater. Sci.*, **62** (2023), 20220320. https://10.1515/rams-2022-0320

19. K. Iqbal, J. Ahmed, M. Khan, L. Ahmad, M. Alghamdi, Magnetohydrodynamic thin film deposition of Carreau nanofluid over an unsteady stretching surface, *Appl. Phys. A*, **126** (2020), 105. https://doi.org/10.1007/s00339-019-3204-6

20. J. Li, L. Liu, L. Zheng, B. Bin-Mohsin, Unsteady MHD flow and radiation heat transfer of nanofluid in a finite thin film with heat generation and thermophoresis, *J. Taiwan Inst. Chem. Eng.*, **67** (2016), 226–234. https://doi.org/10.1016/j.jtice.2016.07.022

AIMS Press